Available online at www.sciencedirect.com
ScienceDirect
Acta Materialia 59 (2011) 3697–3709
Acta MATERIALIA
www.elsevier.com/locate/actamat

The influence of strain rate on the microstructure transition of 304 stainless steel

A.Y. Chen [a,b], H.H. Ruan [b], J. Wang [b], H.L. Chan [b], Q. Wang [b], Q. Li [c], J. Lu [d,*]

[a] School of Material Science & Engineering, Shanghai Institute of Technology, 201400, People's Republic of China
[b] Department of Mechanical Engineering, The Hong Kong Polytechnic University, Hong Kong, People's Republic of China
[c] Physics Department, The Chinese University of Hong Kong, Hong Kong, People's Republic of China
[d] Department of Manufacturing Engineering and Engineering Management, City University of Hong Kong, Hong Kong, People's Republic of China

Received 28 December 2010; received in revised form 4 March 2011; accepted 5 March 2011
Available online 28 March 2011

Abstract

In the top-down approach to tailor the microstructures of materials via plastic deformation, the strain rate plays a significant role. This paper systematically investigates the deformation mechanisms of 304 stainless steel subjected to surface impacts over a wide range of strain rates ($10–10^5\ s^{-1}$). Based on comprehensive analysis of X-ray diffraction and electron microscopy observations, we found that the strain rate between 10 and $10^3\ s^{-1}$ only activated dislocation motions and α′-martensite transformations, resulting in nanocrystallines and ultra-fine grains. However, higher strain rates ($10^4–10^5\ s^{-1}$) produced a high density of twin bundles with nanoscale thickness in the bulk material. The transition from dislocation-mediated mechanism to twinning-mediated mechanism was interpreted in terms of the magnitude of the applied stress, which was calculated from the explicit finite-element simulation with the use of the Johnson–Cook model. A critical twinning stress, determined from the infinite separation of Shockley partials, renders the transition point. Deformation twinning occurs when the applied stress exceeds this critical twinning stress. Larger stress leads to thinner and denser twin lamellae. Conversely, the stress below the transition point can only induce dislocation motions and α′-martensite transformations.

Keywords: Austenitic stainless steels; Microstructure formation mechanism; Phase transformation; Deformation twinning; Strain rate

1. Introduction

Over the past decades, substantial grain refinement from micrometer to submicrometer or nanometer scale has been achieved by various technologies, leading to significant improvement in strength of these materials over their coarse-grained (CG) counterparts. These technologies can be classified into top-down approaches and bottom-up approaches. Severe plastic deformation (SPD) methods are the main top-down approach used to produce ultra-fined grains (UFG, $d < 1$ μm) and nanocrystalline grains (NC, $d < 100$ nm) in bulk materials by exploiting large plastic strains under low strain rates [1]. The grain-refinement mechanisms of most SPD processes are principally dislocation subdivision [2], twin fragmentation [3,4] and phase transformation [5]. It is generally agreed that the equilibrium grain size obtained via dislocation subdivision is not on the nanometer scale (i.e. <100 nm) but generally on the submicron scale. The twin fragmentation and phase transformation of the materials with low stacking fault energy (SFE) are supplementary mechanisms enabling further refinement of grains to the nanometer scale [5].

Apart from SPD, another kind of top-down approach involves surface nanostructuring, which includes shot peening [6], shock loading [7], laser shock processing [8], ballistic impacting [9] and surface mechanical attrition treatment (SMAT) [10]. In these processes, the surface layer of a material is subjected to high-strain-rate deformation, producing nanostructures on the surface and a high density

* Corresponding author.
E-mail address: jianlu@cityu.edu.hk (J. Lu).

1359-6454/$36.00 © 2011 Acta Materialia Inc. Published by Elsevier Ltd. All rights reserved.
doi:10.1016/j.actamat.2011.03.005

of crystalline defects in the subsurface layers, resulting in a much smaller plastic deformation than that produced by SPD [11]. The nanostructuring mechanisms involved in these techniques have been extensively discussed [8,12–14]. For example, Zhang et al. [14] pointed out that the surface nanostructures of AISI 304 SS after SMAT resulted from planar dislocation arrays and twin–twin intersections. Gray [15] observed microtwins in face-centered cubic Al–Mg alloys after explosive loading at surface, which can hardly be twinned under low strain rate due to the very high SFE. These studies showed the preferential occurrence of deformation twinning rather than dislocation slip at higher strain rates.

Nanotwinned (NT) materials have been a focus of research for their novel properties, such as good conductivity and thermal stability [16–19]. Recent discoveries have shown that a high density of twins can not only promote the subdivision of grains to the nanometer scale but also can introduce significant strengthening [16,17]. These findings shed light on a new way to enhance metallic material, i.e. by introducing substantial twins. However, bulk NT materials can only be produced by bottom-up approaches, e.g. electrodeposition [16,17] in the form of thin-film. A top-down approach is in practice more favorable since it can produce bulk NT materials. Strain rate is then one of the key factors. The present study of strain-rate effect spans two extreme cases: either very low strain rates (smaller than $10\ s^{-1}$, e.g. SPD) or extremely high strain rates (larger than $10^5\ s^{-1}$, e.g. laser shock or blast loading). The effect of moderate strain rate has not been investigated.

The main objective of this study is to provide an in-depth understanding of the microstructural evolution and deformation mechanism under a moderate range of strain rates from 10 to $10^5\ s^{-1}$. Since deformation twinning and dislocation slip are competitive mechanisms, understanding the nature of the influence of strain rate on microstructure evolution becomes crucial for developing nanotwinned or nanocrystallized materials [20]. The main objectives of this study are: (i) to provide an in-depth understanding of the microstructural evolution and deformation mechanism over a wide range of strain rates, i.e. $10–10^5\ s^{-1}$; and (ii) to establish a quantitative relationship between strain rate and deformation mechanism, especially on the slipping–twinning transition. AISI 304 stainless steel (SS) sheet was used as the testing material. The effects of strain rate on the formation of nanograins and nanotwins are elaborated in Section 3, followed by a discussion of the transition of the deformation mechanism from dislocation slip to twinning in Section 4.

2. Experimental procedures

The chemical composition of AISI 304 SS is: 0.04 C, 0.49 Si, 1.65 Mn, 7.8 Ni, 16.8 Cr, 0.37 Mo and the balance Fe (all in mass%). Both surfaces of 304 SS specimens (70 mm × 50 mm × 1 mm) were treated by either low-speed SMAT (SMAT-L) or high-speed SMAT (SMAT-H), in which the average impact velocities of the balls are about 0.5 and 10 m s^{-1} [21], respectively. Detailed processing parameters are given in Table 1. In order to reflect the macroscopic plastic strain of the material after SMAT, the residual strain is defined by $\varepsilon = \frac{4}{3}\ln(\frac{V_0}{V_f})$, where V_0 and V_f are the initial and final volume of the treated samples, respectively [11]. To estimate the plastic strain rate induced by ball impact, a simulation model has been developed and applied to 304 SS. A detailed description was given in Refs. [21–23].

The samples for the tensile tests were cut into dog-bone shapes with a gauge length of 30 mm and a width of 6 mm, and tested at room temperature at a strain rate of $6.7 \times 10^{-4}\ s^{-1}$. Four specimens were tested to confirm the repeatability. X-ray diffraction (XRD) was performed to determine the phase composition using a Philips Xpert X-ray diffractometer with Cu Kα radiation. The XRD analyses were carried out along the cross-sectional direction. The samples were carefully prepared by mechanical polishing from the surface to reach the desired depths. The volume fraction of different phases was estimated from the peak integrated intensities $I_{h,k,l}$ after background subtraction. The cross-sections of the specimens were etched by 2 ml HF + 3 ml HNO_3 + 95 ml H_2O and observed by field emission scanning electron microscopy (SEM) using a Hitachi S-4200 microscope. Transmission electron microscopy (TEM) observations were made with a JEM 2010 microscope with an operating voltage of 200 KV. Plane-view and cross-sectional TEM foils were prepared in the same way as in Ref. [14] and ion-thinned at low temperature. Since the treated specimens exhibited depth-dependent microstructures, we used different approaches to obtain quantitatively the distributions of grain size and twin spacing. Specifically, for the SMAT-L sample, the size of grain within the depth of 100 μm was measured from dark-field TEM images. The sizes of the dislocation cell (DC) and the CGs were respectively measured from bright-field TEM images and SEM images for the other regimes. For the SMAT-H sample, the spacing between twin boundaries (λ) was measured from dark-field TEM images and high-resolution (HR) TEM images within the depth of 200 μm and from bright-field TEM images and

Table 1
Processing parameters of SMAT.

Samples	SMAT parameters					
	Vibrating frequency (Hz)	Impact velocity (m s^{-1})	Ball material	Diameter of ball (mm)	Treatment time (min)	Residual strain
SMAT-L	50	~0.5	GGr15	8	40	0.07
SMAT-H	20,000	~10	Bearing steel	3	15	0.2

SEM images for the other regimes. The twin density (TD) at different depths was estimated by calculating the area fraction of grains containing twins with $\lambda < 1$ μm. The dislocation density (DD) was measured from HRTEM images with inverse Fourier transformation (IFT).

3. Microstructure

Multiple deformation mechanisms, such as dislocation motion, twinning and phase transformation, can be triggered in different strain-rate ranges in austenitic stainless steel. In this paper, the SMAT-L sample is deformed under strain rates ranging from $5 \times 10^3\ s^{-1}$ at the surface to $20\ s^{-1}$ at the center. In contrast, the strain rate of the SMAT-H sample varies from 1.2×10^5 to $2 \times 10^4\ s^{-1}$. The dominant deformation mechanism varies from dislocation gliding to martensite transformation and then to deformation twinning with increasing strain rate, which resulted in the UFG and NC material in the SMAT-L sample and the nanotwins in the SMAT-H sample. In the following subsections, we shall elaborate the evidence of these transitions.

3.1. The cross-sectional morphology

A remarkable distinction between the microstructures of the SMAT-L and SMAT-H samples can be observed by SEM after etching the cross-sections. The SMAT-L sample, as shown in Fig. 1a, exhibits non-uniform deformation bands, densely arranged within a depth of 80 μm from the surface, then quickly vanishing after another 70 μm. The grains in the regime close to the surface are mainly UFG, as shown in the inset of Fig. 1a. In contrast, the cross-sectional morphology of SMAT-H sample exhibits a large number of aligned shear bands inside grains with predominant spacing much less than 1 μm, as shown in Fig. 1b. It is worth emphasizing that these finely spaced shear bands were abundant at all depths of the material, indicating the efficiency of the SMAT-H process in altering the microstructure of the bulk stainless steel. It is further noted that the shear bands can parallelly cut through the whole grains (indicated by the solid arrow) or intersect at an angle of about 70° (indicated by the dashed arrow). The differences in the morphologies of the two samples imply that the deformation mechanism changes with the change of strain rate.

3.2. α′-Martensite transformation

Fig. 2 shows XRD patterns of the as-received, SMAT-L and SMAT-H samples. The as-received 304 SS is primarily composed of γ austenite (fcc) and a small amount of α′-martensite (bcc). The α′-martensite transformation occurs in both SMAT-L and SMAT-H samples, as shown in Fig. 2a and b, respectively. However, the amount of α′-martensite differs significantly after the two treatments, as shown in Fig. 2c. The α′-martensite forms more easily during the low-strain-rate SMAT-L process than during the high-strain-rate SMAT-H process. The volume fraction of α′-martensite in the surface of the SMAT-L sample is as high as 95%, as shown in Fig. 2c, which is consistent with Ref. [14]. It is further shown that the volume fraction of α′-martensite gradually reduces to the original value of about 6% at a depth of 180 μm. However, the volume fraction of α′-martensite in the SMAT-H sample is much smaller, varying from about 23% at the surface to 6% at a depth of 150 μm. It is therefore conjectured that the α′-martensite transformation is impeded by the SMAT-H process, which can be attributed to the specific deformation mechanism induced by the high strain rate.

3.3. Nanograins in SMAT-L sample

Nanograins formed on the surface of the SMAT-L sample (Fig. 3a) are α′-martensite with random crystallographic orientations, indicated by the corresponding selected-area diffraction pattern (SAED) shown in Fig. 3b. Fig. 3c shows that the surface grain size is in the range of 2–100 nm, and the mean grain size is approximate 10 nm. At a depth of 50 μm from the surface, both α′-martensite phase and γ-austenite phase

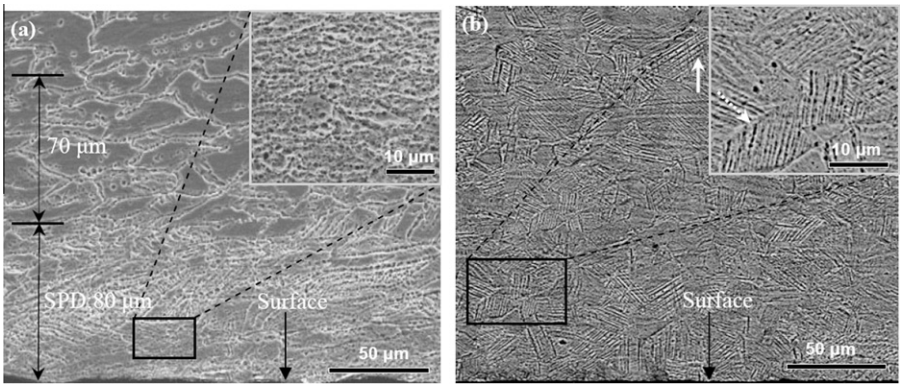

Fig. 1. Cross-sectional SEM observations of (a) SMAT-L and (b) SMAT-H samples.

are observed, as illustrated in Fig. 3d–g. This result is consistent with the XRD analysis. Fig. 3e and f are dark-field TEM images diffracted from the spots "B" and "C" in the SAED pattern in Fig. 3d, showing the equiaxed grains of α′-martensite and γ-austenite, respectively. The mean grain size of α′-martensite is about 60 nm, much smaller than that of the γ-austenite (200 nm), as shown in Fig. 3g. The nanosized α′-martensite is still the primary component at this depth. However, the larger γ-austenite grains are uniformly distributed among them, resulting in a bimodal grain size distribution. It is noted that no other phase can be observed under TEM and XRD, indicating that only $\gamma \rightarrow \alpha'$ transformation occurs in SMAT-L sample. In comparison, the surface microstructures of the SMAT-H sample are shown in Fig. 4. Both α′-martensite and γ-austenite phases can be identified in Fig. 4a. Nevertheless, both the mean grain sizes and distribution ranges, as summarized in Fig. 4b, are much larger than those of the SMAT-L sample. Combined with the XRD analysis, the above comparison indicates that the higher strain rate is not effective in reducing grain size due to hindering effect of the α′-martensite transformation, but is nevertheless the main mechanism producing nanograins in the SMAT-L sample.

With increasing depth, the grain size of the SMAT-L sample gradually increases from a few nanometers to hundreds of nanometers within 150 μm. At depths of 150–350 μm, a large number of DCs with a high density of tangled dislocations is observed in most grains, as shown in Fig. 5. Some microtwins can also be found at depths of 200–300 μm, but the number of microtwins is small in comparison with that of the DCs. To recapitulate, the microstructures of the SMAT-L sample are characterized by a multi-modal grain size distribution with a dual-phase structure. For the whole thickness, the volume fraction of NC and UFG material is about 30%; CGs with submicron-sized DCs comprise the remaining volume.

3.4. Nanotwins in the SMAT-H sample

In contrast to the NC/UFG structure of the SMAT-L sample, the SMAT-H sample possesses more complex microstructures, which are primarily austenite nanotwins as well as a small fraction of α′-martensite and ε-martensite (hcp). Fig. 6a is a bright-field TEM image revealing a large number of deformation twins at a depth of 50 μm. These deformation twins mostly nucleate from grain boundaries and grow into the grain interior. Some of them do not transect the entire grain but terminate in the grain interior. Fig. 6c shows the magnification of the circled area in Fig. 6a. The SAED pattern of Fig. 6c, indexed in Fig. 6b, shows composite diffractions of γ-austenite, twin, ε-martensite and α′-martensite with the zone axis $[\bar{1}10]_{\gamma}//[1\bar{1}0]_{twin}//[11\bar{2}0]_{\varepsilon}//[1\bar{1}1]_{\alpha'}$. This orientation relationship is the well-known Kurdjumov–Sachs (K–S) relationship. The dark-field images in Fig. 6d–f are obtained from diffraction spots "1", "2" and "3" in Fig. 6b, showing the morphologies of nanotwins, ε-martensite and α′-martensite, respectively. Fig. 6d shows dense bundles of nanoscale twins with large numbers of dislocations. Statistical measurements indicate that the twin thickness λ varies between 2 and 50 nm, with an average value of about 20 nm, as shown in the inset of Fig. 6d. These NT structures are found in most grains. Fig. 6e shows ε-martensite platelets of very small thickness (~45 nm). It is identified that the impact-induced {0 0 0 1} habit plane of ε-martensite phase matches the orientation relationship $[11\bar{2}0]_{\varepsilon}//[\bar{1}10]_{\gamma}$. The

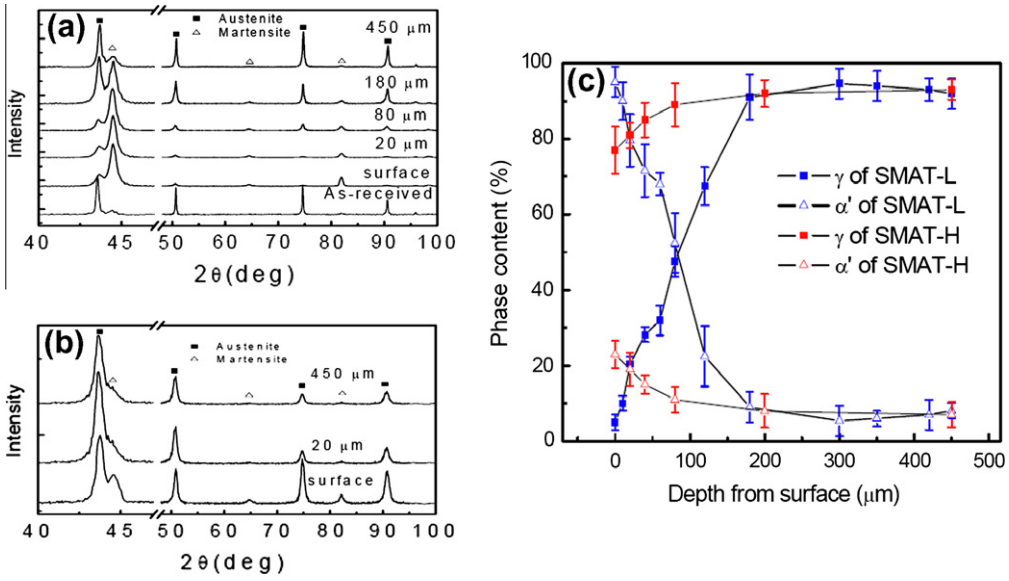

Fig. 2. (a and b) XRD patterns of the as-received, SMAT-L and SMAT-H samples, respectively; (c) phase content at different depths of the SMATed samples.

morphology of α′-martensite can be classified into two types, as indicated in Fig. 6f. The first type comprises martensite laths of submicron thickness distributed along twin lamellae (marked by α′1). The second is island-shaped α′-martensite inside twin lamellae (marked by α′2). These α′-martensite islands originate from the fragmentation of deformation twins. In studying the high-strain-rate compression of stainless steel, Staudhammer et al. [24] designated both types of α′-martensite as stress-assisted martensite, whose shape is different from that of strain-induced material. The statistical distribution of the thickness of α′-martensite lath is given in the inset of Fig. 6f. The average thickness is about 120 nm. In the subsurface layer of SMAT-H sample, ε-martensite and α′-martensite phases are found, and we speculate that the deformation mechanisms occurring in this layer are mainly deformation

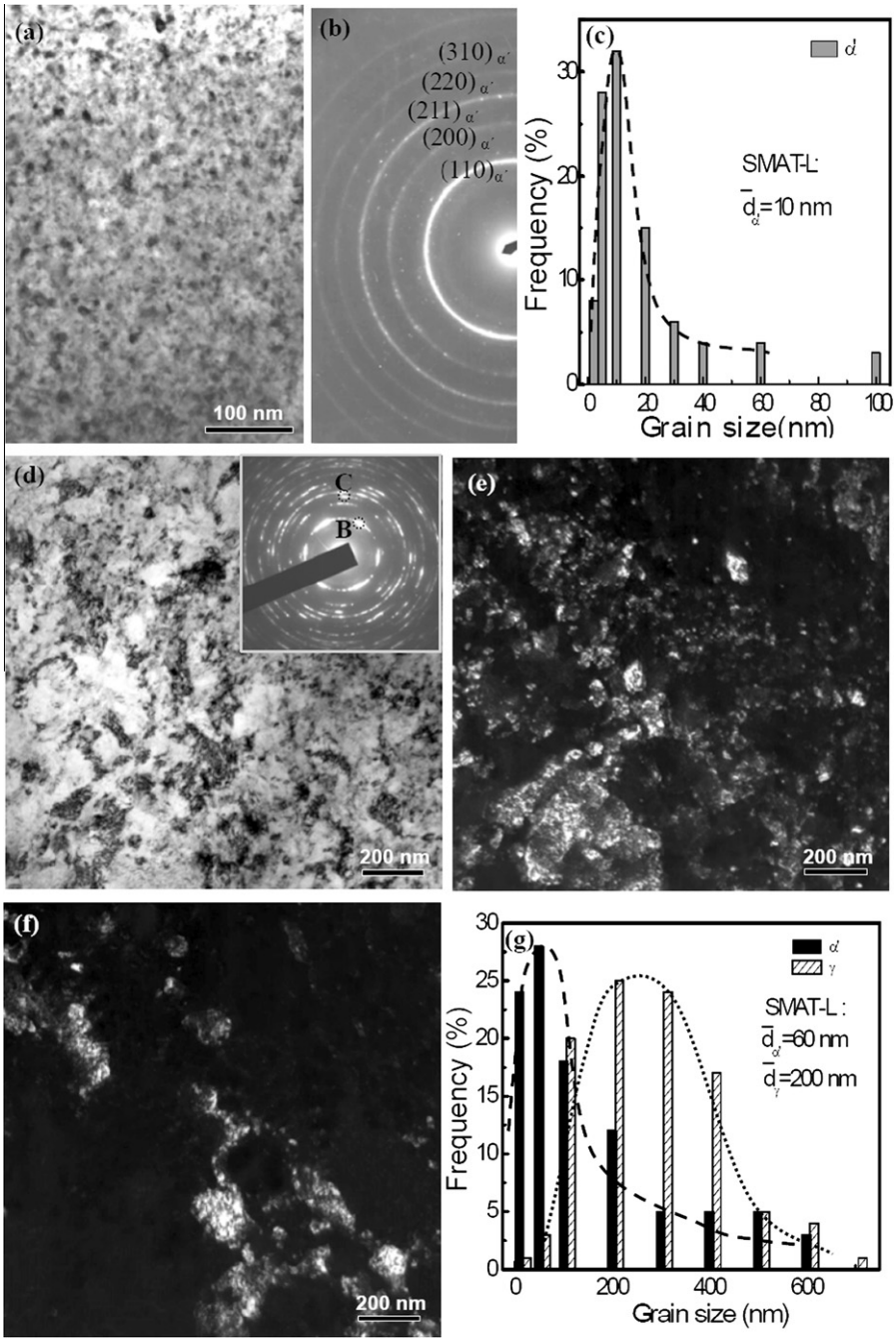

Fig. 3. Nanostructures of the SMAT-L 304 SS: (a) bright-field TEM image; (b) selected-area electron diffraction (SAED) pattern; (c) statistical distribution of grain size on the surface, respectively. (d)–(g) Nanostructure at a depth of 50 μm from the surface: (d) bright-field TEM image and SAED pattern; (e and f) dark-field TEM images corresponding to the diffraction zone marked "B" and "C" in the SAED pattern of (d), respectively. (g) Statistical distribution of grain size of α′-martensite and γ-austenite phase, respectively.

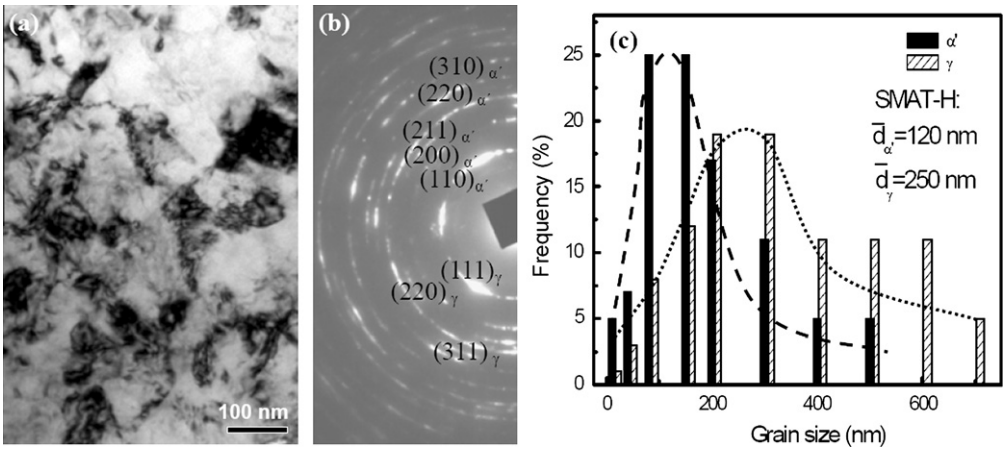

Fig. 4. Microstructures of the SMAT-H 304 SS at surface: (a) bright-field TEM; (b) SAED pattern; (c) statistical distribution of grain size.

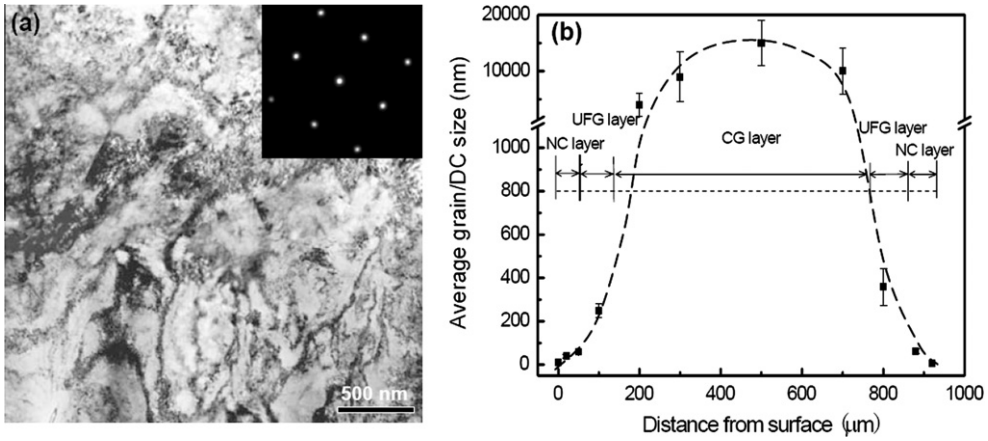

Fig. 5. (a) Bright-field TEM images and the SAED pattern of the SMAT-L samples at a depth of 300 μm, showing the UFG dislocation cells (DCs). (b) Grain size/DC distribution in the SMAT-L sample.

twinning, followed by some $\gamma \rightarrow \varepsilon$ transformation and twin $\rightarrow \alpha$ transformations.

In order to investigate the details of nanotwins and nano ε-martensite, HRTEM observations of the outlined region in Fig. 6c are shown in Fig. 7. Fig. 7a shows that the twin is composed of several atomic layers about 11 nm thick. As indicated in the inset of Fig. 7a, strong diffraction spots appear with respect to the {1 1 1} plane, and diffuse spots in the [1 1 1] direction, indicating the formation of deformation twins and stacking faults on the {1 1 1} plane. The corresponding inverse Fourier transform (IFT) image (Fig. 7b) exhibits high-density dislocations inside the nanotwin lamellae and at twin boundaries, which is distinct from the growth twin structure where less dislocation exists [17]. Some of these dislocations are found to be Shockley partial dislocations. A twinning mechanism by partial dislocation dissociation has been predicted by molecular dynamics simulations in nanocrystalline Al [25] and experimentally evidenced in nanocrystalline aluminum [26] and copper [27]. Fig. 7c and the associated IFT image (Fig. 7d) show the coexistence of ε-martensite grains, twin lamellae and stacking faults. The ε-martensite phase is not detected in the XRD patterns of the SMAT-H sample, since they are exceptionally small and scarce. The TEM image and HRTEM images clearly reveal that ε-martensite platelets are a few nanometers in size. The ε-martensite platelets and deformation twins are formed by different stacking sequences of stacking faults on close-packed planes. The change in stacking sequence of the close-packed (1 1 1) planes from ABCABC to ABABAB is achieved by passing partial Shockley dislocations of Burgers vector $1/6[1\,1\,\bar{2}]_{\gamma}$ on every two $(1\,1\,1)_{\gamma}$ planes [28]. The sequence of stacking faults is irregularly overlapped at first and then changes gradually to the regular sequence. Correspondingly, the diffraction pattern changes from fcc matrix to broadened streaks first, and then to the pronounced intensity maxima appearing on these streaks. This procedure is clearly shown in Fig. 7e–g, where the SAED patterns and IFT images are taken at square regions "A", "B" and "C" in Fig. 7c, respectively. The above

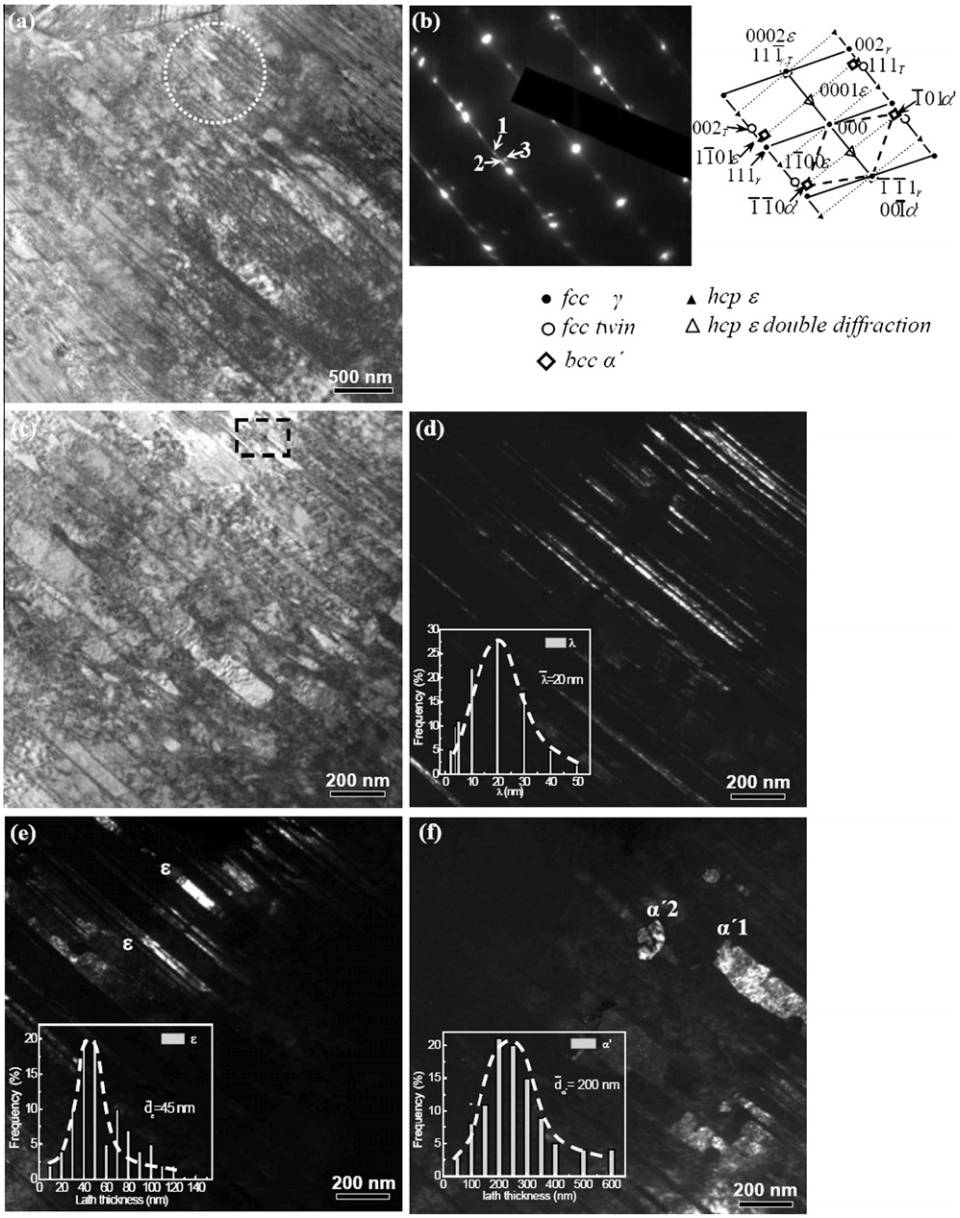

Fig. 6. TEM images of SMAT-H sample at 50 μm depth: (a) bright-field TEM; (b) SAED pattern and indexed pattern, showing the ε-martensite (hcp), α′-martensite (bcc), and twin (fcc) with the zone axis of $[\bar{1}10]_\gamma//[1\bar{1}0]_{twin}//[11\bar{2}0]_\varepsilon//[1\bar{1}1]_{\alpha'}$; (c) bright-field TEM of the magnification of the circle regime in (a); (d)–(f) dark-field TEM images, corresponding to the diffraction patterns "1", "2" and "3" in (b), respectively; The insets of (d)–(f) are the statistical distribution of lath thickness of α′-martensite phase, ε-martensite phase and twins.

observations show that the deformation twinning is usually accompanied by ε-martensite transformation at high strain rates, corroborating the $\gamma \rightarrow$ nanotwin/ε-martensite $\rightarrow \alpha'$-martensite transformation sequence occurring in the SMAT-H sample, in contrast to the direct $\gamma \rightarrow \alpha'$-martensite transformation observed in the SMAT-L sample.

Intersections of two twinning systems are also observed at large depths. A typical twin–twin intersection observed at a depth of 300 μm is shown in Fig. 8a, in which the angle between the primary and the conjugate twins is 70.5°, corresponding to the simple shear sliding of $a/\sqrt{2}$ in the $[\bar{1}10]$ plane. The overall microstructure of SMAT-H sample features the high density of twins in the entire thickness of the sheet with λ from a few nanometers in the subsurface to hundreds of nanometers in the center. A large number of dislocations were also found associated with these deformation twins. They are also the deformation byproduct, which can on the one hand assist the formation of twins and on other hand impede twin growth, as will be discussed in Section 4.2. The crucial structure parameters of the twinned materials, i.e. distributions of the twin thickness λ and the twin density (TD), are shown in Fig. 8b. The value of λ varies from 20 nm at a depth of 50 μm to about 350 nm in the center.

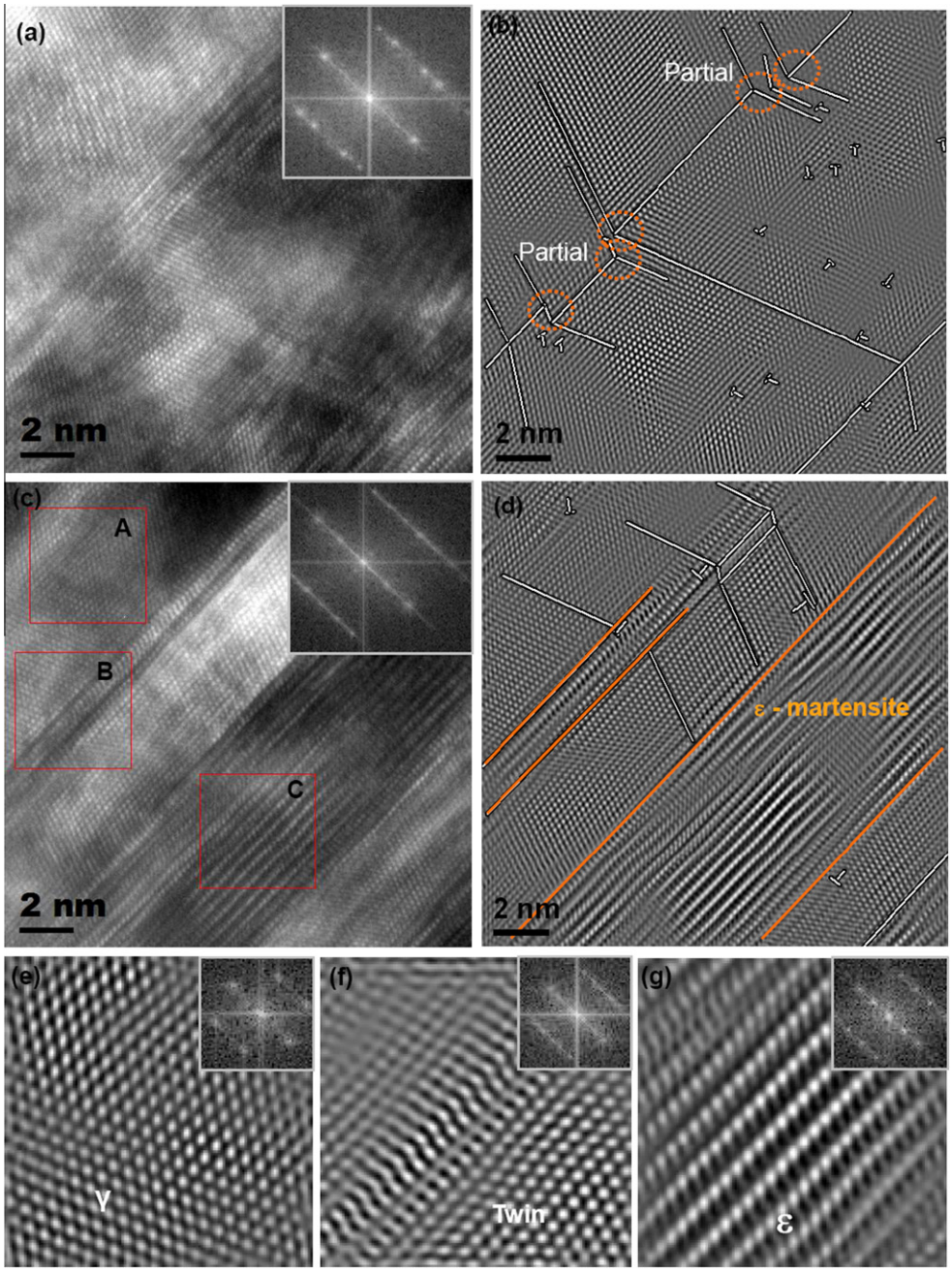

Fig. 7. HRTEM images of the SMAT-H sample at a depth of 50 μm from surface: (a and b) HRTEM image and the corresponding inverse Fourier transformation (ITF) image viewed from the [011] zone axis, showing deformation nanotwins and dislocations inside the twin; (c and d) HRTEM image and the corresponding ITF image viewed from the [011] zone axis, showing deformation nanotwins and ε-martensite, indicated by white lines and orange lines, respectively; (e)–(g) high magnification of the rectangle A, B, C in (c), showing the austenite, twin and ε-martensite, respectively.

Correspondingly, the twin density varies from about 65% at a depth of 50 μm to 40% in the center. Similar nanoscale twins were observed in various steels after other mechanical processes, such as laser-shocked 304 SS, ECA-Ped 316L SS and cold-worked austenite steel [8,29,30]. However, the deformation twins produced by the present high-strain-rate process have the smallest thickness and the largest density, which spreads to all the depths of the bulk material.

3.5. Mechanical properties

Mechanical properties are the embodiment of a material's microstructure. Corresponding to the depth-dependent microstructures discussed above, we investigated the depth-dependent hardness, which is summarized in Fig. 9a for both SMAT-L and SMAT-H samples. The maximum hardness of the SMAT-L specimen is 502 MPa at the surface, which is mainly attributed to the strengthening of

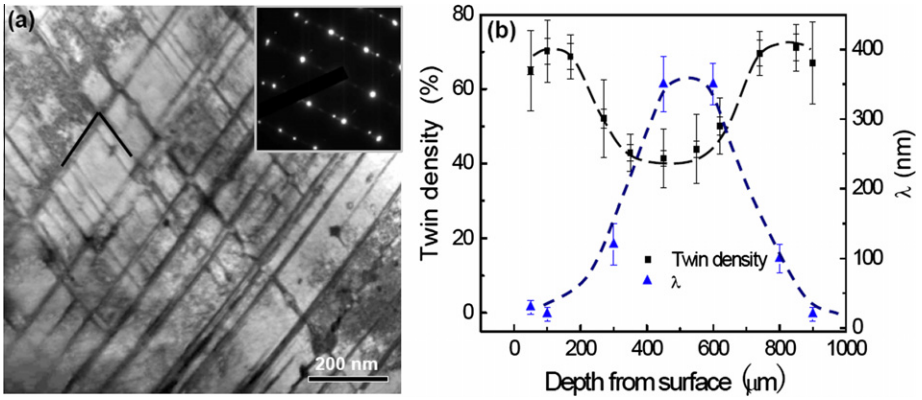

Fig. 8. (a) Bright-field TEM images and the corresponding SAED pattern of the SMAT-H samples at a depth of 300 μm, showing the intersection of twins; (b) twin density and λ distributions in the SMAT-H sample.

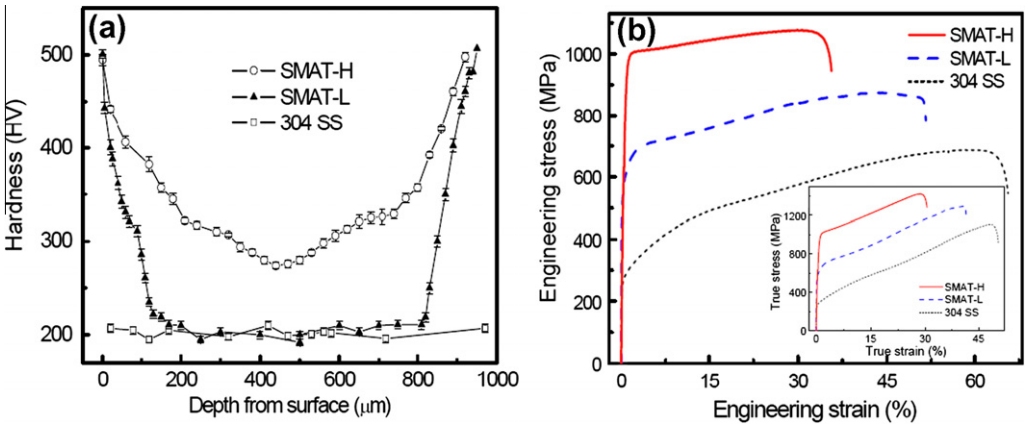

Fig. 9. Mechanical properties of the SMAT samples and as-received 304 SS: (a) hardness distribution with depth; (b) engineering stress–strain curves. The inset shows true stress–strain curves.

nanograins, especially the nanosized α′-martensite grains. The microhardness then decreases to the original value of the as-received 304 SS (200 MPa) at a depth of 180 μm due to the decrease in volume fraction of the α′-martensite and the increase in grain size. This result is consistent with the microstructures of the SMAT-L steel. However, for the SMAT-H sample, since the deformation twins remain abundant even in the middle layer, the whole bulk material was notably strengthened and the microhardness varies from 495 MPa at the surface to about 274 MPa at the center.

Fig. 9b shows the tensile curves of the as-received, SMAT-L and SMAT-H samples. In most cases, the materials processed by SPD exhibit very high strength but generally low ductility regardless of processing temperature [1,30,31]. However, with our process, a good combination of high yield strength and high ductility has been achieved, which is most likely due to the higher strain-hardening capacity, as shown in the inset of Fig. 9b. The superior mechanical properties can be attributed to the complex microstructure induced by the SMAT processes, such as the bimodal grain size distribution as shown in Figs. 5b and 8b. In this case, the nanosized grains provide the very high strength, while the micronsized grains provide the significant strain-hardening capacity through dislocation pile-up as discussed in Refs. [32,33].

It is noted that the SMAT-H sample is stronger than the SMAT-L sample, which is in agreement with the hardness result. The reason for this difference between the SMAT materials is that the SMAT-H process can induce large numbers of deformation twins at all depths of the material, whereas the SMAT-L process can only affect down to 180 μm. The deformation twins induced by the SMAT-H process play a similar role as grain boundaries in blocking dislocation motions [16,17]. Thus the more abundant and finer the twins, the higher the strength.

4. Discussions

Table 2 summarizes the microstructures and deformation mechanisms produced by the two SMAT process. From the above microstructure analysis, we note that: (i) deformation twinning is predominant at strain rates of 10^4–10^5 s^{-1}; (ii) α′-martensite transformation can be

Table 2
Microstructure characteristics of the SMAT-L and SMAT-H samples.

Sample	Depth (μm)	SR[a] ($\times 10^4$)	RS[b] ($\times 10^{-2}$)	DD[c] ($\times 10^{16}$ m^{-12})	TEM microstructures	Deformation mode
SMAT-L	0	0.4	1.0	~35	Nano α′	γ → α′
	50	0.5	1.7	~40	Nano α′ (P[d]), nano γ	γ → dislocation
	100	0.01	1.3	~23	UFG γ (P), UFG α′, pile-up dislocation	γ → twin
	300	0.002	0.4	–	Tangled dislocations (P), twins,	
SMAT-H	0	9	5.3	~5	UFG γ (P), UFG α′, pile-up dislocation	γ → twin
	50	12	6.6	~2	Nanotwins (P), nano α′, nano ε, tangled dislocation	γ → α′ γ → ε
	100	7	6.8	~2	Nanotwins (P), nano α′, nano ε, tangled dislocations	γ → twin → α′ γ → ε → twin
	300	2	4.2	–	UFG twins (P), nano ε, tangled dislocations	γ → dislocation

[a] SR, Strain rates.
[b] RS, Residual strain.
[c] DD, Dislocation density.
[d] P, Primary constituent.

retarded at high strain rates; (iii) the dislocation subdivision can only achieve UFG, and the α′-martensite transformation is necessary to obtain nanograins ($d < 100$ nm). In the following, we seek an interpretation of this strain-rate effect by assuming that different deformation mechanisms are induced by different stress levels.

Christian and Mahajant [7] postulated that the necessary condition for deformation twinning in fcc metals is that the local stress resulting from stress concentration should be elevated to levels higher than the critical twinning stress (CTS). Byun et al. [34] examined the relationship of the equivalent stress and the deformation-induced microstructure in 316 LN stainless steels by using a disk-bend method. The experimental and theoretical results demonstrated that austenitic steels deform by twinning when a sufficiently high stress (i.e. larger than CTS) can be reached irrespective of which loading method is used [31,35–37]. The CTS can be achieved by dynamic strain aging, large plastic strain and/or high strain rate [18,34]. Although the existence of the CTS for fcc material has been well recognized, the tendency to substitute twinning for slip, and the actual magnitude of the twinning stress, has been less studied, especially the strain-rate dependence of twinning stress.

4.1. Critical twinning stress

The occurrence of dislocation substructures and twins is influenced by the width of partial dislocation separation caused by the resolved shear stress τ [29,35,37]. Dissociation of a perfect dislocation on {1 1 1} plane into two Shockley partial dislocations can be expressed as $\frac{a}{2}[1\bar{1}0] = \frac{a}{6}[2\bar{1}\bar{1}] + \frac{a}{6}[1\bar{2}1]$, where $\frac{a}{2}[1\bar{1}0]$, $\frac{a}{6}[2\bar{1}\bar{1}]$ and $\frac{a}{6}[1\bar{2}1]$ are the Burgers vectors of the perfect, the leading and the trailing partial dislocations, respectively. Byun [35] showed that in low-SFE materials, the equilibrium separation distance w of Shockley partials depends on the SFE γ_{SFE} and the shear stress τ, which is given by:

$$w = \frac{Gb_p^2}{\pi(2r_{SFE} - \tau b_p|\sin\theta_2 - \sin\theta_1|)} \times \left(\cos\theta_1\cos\theta_2 + \frac{\sin\theta_1\sin\theta_2}{(1-v)}\right), \quad (1)$$

where b_p is the value of the Burgers vector of a Shockley partial dislocation, G is the shear modulus, v is Poisson's ratio, θ_1 and θ_2 are respectively the angles of the Burgers vectors of the leading and trailing partial dislocations referring to the Burgers vector of the perfect dislocation. Eq. (1) indicates that the width of a stacking fault increases with increasing shear stress and approaches infinity when the shear stress exceeds a critical value. This situation corresponds to the scenario that only the leading partial dislocations emit from the highly stressed region, which is the necessary condition for deformation twinning. Therefore, the stress for the infinite separation of Shockley partials can be regarded as the CTS, which satisfies:

$$(2r_{SFE} - \tau_{CTS} b_p|\sin\theta_2 - \sin\theta_1|) = 0. \quad (2)$$

Since the resolved shear stress τ is maximized when the angles θ_1 and θ_2 are $-30°$ and $30°$, respectively, corresponding to perfect dislocation dissociation on the {1 1 1} plane [37], the CTS is simplified by:

$$\tau_{CTS} = \frac{2\gamma_{SFE}}{b_p}. \quad (3)$$

By assuming an average Schmid factor 0.326 for polycrystalline stainless steel, the critical equivalent stress (σ_T) for twinning can be given by:

$$\sigma_T = 6.13\frac{\gamma_{SFE}}{b_p}. \quad (4)$$

For the 304 stainless steel ($\gamma_{SFE} = 16$ mJ m^{-2}, and $b_p = 0.147$ nm), Eq. (4) predicts the critical equivalent stress for twinning to be about 584 MPa. The exact critical

equivalent stress should vary with Schmid factor for different slip systems [38]. When the resolved shear stress reaches CTS, the slipping–twinning transition occurs.

To quantitatively analyze the stress experienced by the material during SMAT, the empirical rate-sensitivity Johnson–Cook model [39] was adopted:

$$\sigma_T = [A + B\varepsilon^n]\left[1 + C\ln\left(\frac{\dot{\varepsilon}}{\dot{\varepsilon}_0}\right)\right], \quad (5)$$

where σ_T is equivalent stress, ε is equivalent plastic strain, $\dot{\varepsilon}$ is plastic strain rate, $\dot{\varepsilon}_0$ is the reference strain rate for a quasi-static test, n is the work-hardening exponent, and A, B, C and m are constants. The parameters for 304 SS are $A = 300$ MPa, $B = 1.477$ MPa, $n = 0.72$, $C = 0.02$, $\dot{\varepsilon}_0 = 10^{-3}$ [22,23]. We established an axisymmetric model and simulated the normal impact of a rigid ball onto the sample surface. The contour maps of equivalent stresses are plotted in Fig. 10a and b for SMAT-L and SMAT-H processes, respectively. The equivalent stress in the SMAT-L sample is in the range of 280–560 MPa, as shown in Fig. 10a, which is lower than the critical equivalent stress for deformation twinning. However, the equivalent stress in the SMAT-H sample is apparently higher than the critical equivalent stress. The equivalent stress is as high as 1 GPa to a depth of 50 μm and then gradually decreases to 590 MPa in the center, as shown in Fig. 10b. The experimental observation matches the theoretical calculation, confirming that our estimation of critical twinning stress is reasonable. Comparing the stress distribution (Fig. 10) with the TEM observations (Figs. 5–8), the deformation mechanisms may be correlated to the stress level as: (i) dislocation slip is dominant at the equivalent stress lower than 400 MPa (corresponding to strain rates smaller than 10^2 s^{-1}); (ii) α′-martensite transformation is activated in the stress range of 400–560 MPa (corresponding to strain rates of 10^2–10^3 s^{-1}); and (iii) deformation twins are initiated at stresses higher than 584 MPa (corresponding to strain rates larger than 10^4 s^{-1}). Since the plastic strain in the SMAT process is very small, as given in Table 1, much smaller than that of SPD processes, we shall consider that these stress levels are mainly attributed to the different strain rates.

4.2. Critical twinning nucleus size

Formation of stable deformation twins comprises nucleation of twin embryos and their subsequent growth when the applied stress is larger than the CTS. The critical twin nucleus thickness, λ_c, depends on the twin boundary energy (γ_{TB}) and the driving stress of twin nucleation. The relation between λ_c and the equivalent stress is given by [20,36]:

$$\lambda_c = \frac{5\pi}{4}\frac{G\gamma_{TB}}{\sigma_T^2}. \quad (6)$$

Eq. (6) indicates that the twin nucleus size is inversely proportional to the stress. Due to the uncertainties of γ_{TB}, we select values of γ_{TB} in the range of $2\gamma_{SFE}$–$10\gamma_{SFE}$ as introduced in Ref. [36]. Comparing the nucleus size with the experimentally measured twin size, as shown in Fig. 11, can be seen that the measured λ is close to λ_c at high stress but considerably deviates from λ_c at low stress. Venables [40] pointed out that the resistance to twin growth increases with the dislocation density. Therefore larger dislocation density leads to thinner twins. It is observed that the dislocation density in the SMAT-H sample is $2\sim5 \times 10^{16}$ m^{-2} up to a depth of 100 μm (shown in Table 2), even higher than that produced by other SPD processes [11,41]. Such high dislocation density may impede the growth of twins. In addition, larger strain rates usually imply smaller lifetimes [21], limiting the time for the growth of twins. The spatial and temporal limitation under high strain rates results in a very small twin thickness. Conversely, for the lower strain rate and smaller stress, the twin nucleus has plenty of room and time to grow, resulting in an increase in the difference between the measured twin thickness and the calculated thickness of the twin nucleus shown in Fig. 11.

Moreover, it should be noted that the twin lamellae are so fine that no further fragmentation of the deformation twins occurs. Most of the nanotwins were simply parallel

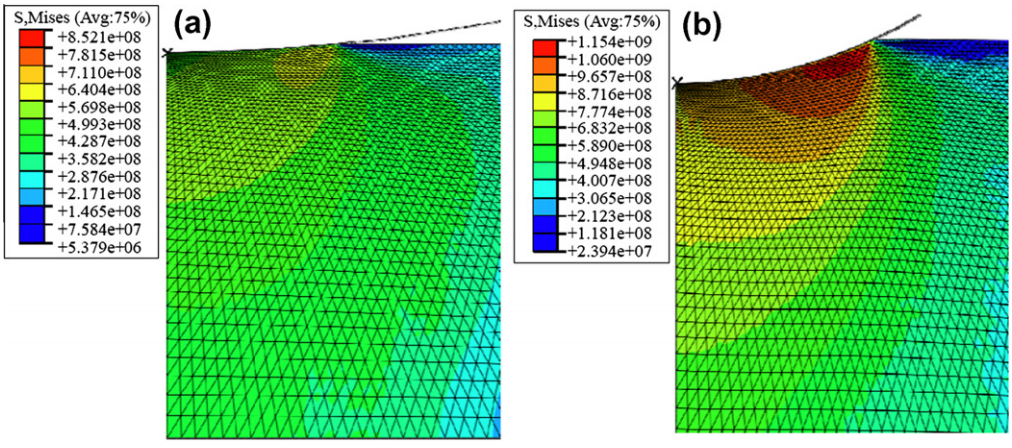

Fig. 10. Contour map distributions of equivalent stress in (a) SMAT-L and (b) SMAT-H samples.

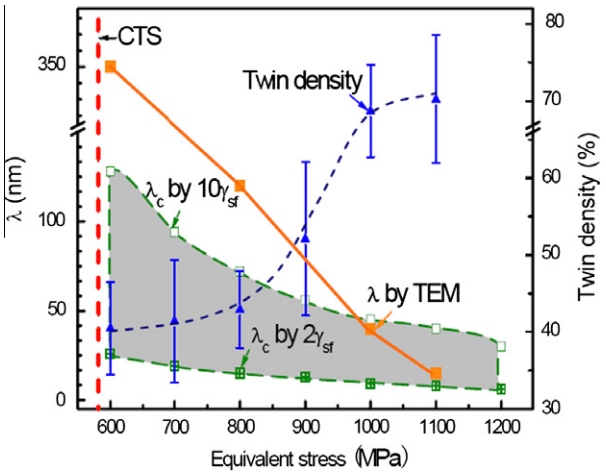

Fig. 11. The dependence of critical twin thickness (λ_c) and twin density with equivalent stress in the SMAT-H sample.

aligned in the gains. In previous reports, deformation twins play a significant role in refining grains via the interactions of twin bundles and dislocations, resulting in the formation of nanograins, as evidenced in dynamically plastically deformed copper [4] and ECAPed SS [5]. In our case, the high density of nanotwins remains stable during the SMAT-H process. The preservation of nanotwins is attributed to the high strain rate, large dislocation density and very small strain. As discussed above, the high strain rate induces much finer twin lamellae and a larger twin density, resulting in nanotwin stability. However, the almost strain-free deformation caused by SMAT may be the most important reason for the formation of nanotwins instead of NC grains since no obvious macroscopic plastic deformation cuts the twin lamellae, which is the fundamental difference from the large strain in the SPD processes.

4.3. Nanocrystalline formation

An obvious strain rate effect on the refinement of initial CG to NC and UFG microstructures occurs at strain rates of 10–10^3 s^{-1}. Two mechanisms operate: (i) dislocation activities, such as accumulation, interaction, tangling and spatial rearrangement; and (ii) α′-martensite transformation. With mechanism (i), refinement of CG is dominated by dislocation slip to form various dislocation structures, including DCs, walls and geometrically necessary boundaries [4,41]. The DCs gradually transform into subgrains with the eventual grain size determined by the DC size. The size of DC (d_{DC}) depends upon the shear stress (τ) according to [41]:

$$d_{DC} = \frac{KGb}{(\tau - \tau_0)} \approx \frac{KGb}{\tau} \approx \frac{KGb}{0.326 \times \sigma_T}, \quad (7)$$

where K is a constant (normally taken as 10) [41], and τ_0 is the internal frictional resistance to the relative sliding of atomic layers. The d_{DC} is calculated to be 0.8–1.6 μm when the applied external stress varies from 560 to 280 MPa. This means that grains resulting from dislocation activity cannot be finer than 0.8 μm. Therefore, α′-martensite transformation must operate to produce finer grains. Figs. 2, 3 and 8a show that 70% of nanosized grains ($d < 100$ nm) are α′-martensite in the SMAT-L sample. This result suggests that α′-martensite transformation is more effective in refining grains down to the nanometer scale. The stress-mediated α′-martensite transformation requires the assistance of dislocation pile-up [34]. At a limited strain, a sufficient density of dislocations should be induced by large strain rates. Up to a depth of 100 μm in the SMAT-L sample, the dislocation density is 2.3–4 × 10^{17} m^{-2}, which is even larger than that of other nanocrystalline metals,—for example, the dislocation density is about 10^{10} m^{-2} in shock-loaded 316L SS and about 10^{15} m^{-2} in Cu after multiple impacts at low temperature [11,41]. Such high dislocation density promotes the α′-martensite nucleation to form nanograins. However, the α′-martensite transformation is retarded by the further elevated strain rate, as observed in the SMAT-H sample. This can partly be attributed to the elevated temperature in the high-strain-rate deformation [42]. A similar phenomenon was also found by strain-controlled tensile testing [43,44]: the α′-martensite transformation occurred at smaller strains with higher strain rates and then diminished as the strain rate increased further. In the strain-controlled quasi-static tensile test, α′-martensite transformation occurs at a stress of over 400 MPa after significant strain hardening [42,43]. This indicates that the critical stress for the nucleation of α′-martensite must be around 400 MPa under either the stress-mediated or the strain-mediated process. For 304 SS at zero plastic strain, this stress corresponds to a strain rate of 10^2. In noting that a strain rate larger than 10^4 leads to nanotwins, we conclude that strain rates of the order of 10^2–10^3 are the most effective way to induce α′-martensite transformation and nanograins.

5. Conclusions

The influence of strain rate on microstructure and mechanical properties of the 304 SS are systematically investigated. The transition from dislocation slip to deformation twinning is analyzed. The results are summarized as follows:

(1) Deformation mechanisms via $\gamma \rightarrow$ twin, $\gamma \rightarrow \alpha'$ and $\gamma \rightarrow \varepsilon$ have been observed under high strain rates of 10^4–10^5 s^{-1}, and deformation twinning is dominant. In contrast, dislocation activities and the direct $\gamma \rightarrow \alpha'$ transformation are the dominant deformation mechanisms under lower strain rates of 10–10^3 s^{-1}.
(2) An analytical model is proposed to calculate the critical twinning stress, which is 584 MPa for 304 SS, corresponding to a strain rate of 10^4 s^{-1}. By comparing the stress distributions obtained by finite-element simulation and the microstructure observation, it is confirmed that the critical twinning stress accurately

delineates the transition from dislocation slip to deformation twinning. We further conjecture that α′-martensite transformation occurs in a medium stress range of about 400–500 MPa (corresponding to strain rates of 10^2–10^3 s^{-1}). If the equivalent stress is lower than 400 MPa, dislocation activities are dominant.

(3) If the applied stress is much larger than the CTS, which can be achieved with a sufficiently high strain rate (say 10^5 s^{-1}), a large density of deformation twins with thicknesses as small as 20 nm can be produced. These nanoscale twins do not grow after nucleation owing to spatial and temporal limitations. Therefore, the thickness of these nanotwins agrees with the theoretical estimate of the size of the twin nucleus.

(4) Dislocation activities can only form UFGs and/or ultra-fine DCs, while α′-martensite transformation forms nanoscale grains. For a limited plastic strain, a strain rate in the range of 10^2–10^3 s^{-1} can produce a very large dislocation density (about 10^{17} m^{-2}), leading to a large number of nucleation sites for α′-martensite transformation. Nevertheless, the higher strain rate tends to impede α′-martensite transformation due to deformation twinning.

Acknowledgements

The authors are grateful to the Research Grant Council (RGC) for the financial support of grant number CityU8/CRF/08 and the Hong Kong Innovation and Technology Commission (ITC) for financial support of the research project (No. ITP/004/08NP).

References

[1] Valiev RZ, Islamgaliev RK, Alexandrov IV. Prog Mater Sci 2000;45:103.
[2] Iwahashi Y, Horita Z, Nemoto M, Langdon TG. Acta Mater 1998;46:3317.
[3] Qu S, An XH, Yang HJ, Huang CX, Yang G, Zang QS, et al. Acta Mater 2009;57:1586.
[4] Li YS, Tao NR, Lu K. Acta Mater 2008;56:230.
[5] Huang CX, Gao YL, Yang G, Wu SD, Li GY, Li SX. J Mater Res 2006;21:1687.
[6] Lindemann J, Buque C, Appel F. Acta Mater 2006;54:1155.
[7] Christian JW, Mahajant S. Prog Mater Sci 1995;39:1.
[8] Lu JZ, Luo KY, Zhang YK, Sun GF, Gu YY, Zhou JZ, et al. Acta Mater 2010;58:5354.
[9] Zhen L, Li GA, Zou DL, Shao WZ. Mater Sci Eng A 2008;489:213.
[10] Lu K, Lu J. Mater Sci Eng A 2004;375–377:38.
[11] Sencer BH, Maloy SA, Gray GT. Acta Mater 2005;53:3293.
[12] Murr LE, Meyers MA, Niou CS, Chen YJ, Pappu S, Kennedy C. Acta Mater 1997;45:157.
[13] Murr LE, Trillo EA, Bujanda AA, Martinez NE. Acta Mater 2002;50:121.
[14] Zhang HW, Hei ZK, Liu G, Lu J, Lu K. Acta Mater 2003;51:1871.
[15] Gray GT. Acta Met 1988;36:1745.
[16] Lu K, Lu L, Suresh S. Science 2009;324:349.
[17] Lu L, Chen X, Huang X, Lu K. Science 2009;323:607.
[18] Karaman I, Kulkarni AV, Luo ZP. Philos Mag 2005;85:1729.
[19] Lu L, Shen Y, Chen X, Lu K. Science 2004;304:422.
[20] Zhang Y, Tao NR, Lu K. Scr Mater 2009;60:211.
[21] Chan HL, Ruan HH, Chen AY, Lu J. Acta Mater 2010;58:5086.
[22] Ruan HH, Chen AY, Lu J. Mech Mater 2010;42:559.
[23] Ruan HH, Chen AY, Chan HL, Lu J. Mech Mater 2010;42:698.
[24] Staudhammer KP, Murr LE, Hecker SS. Acta Metall 1983;31:267.
[25] Yamakov V, Wolf D, Phillpot SR, Mukherjee AK, Gleiter H. Nat Mater 2002;1:1.
[26] Chen MW, Ma E, Hemker KJ, Wang YM, Cheng X. Science 2003;300:1275.
[27] Huang CX, Wu SD, Zhang ZF, Li GY, Li SX. Acta Mater 2006;54:655.
[28] Huang CX, Yang G, Gao YL, Wu SD, Li SX. J Mater Res 2007;22:724.
[29] Yapici GG, Karaman I, Luo ZP, Maier HJ, Chumlyakov YI. J Mater Res 2004;19:2268.
[30] Saller G, Hahn KS, Scheu C, Clemens H. Mater Sci Eng A 2006;427:246.
[31] Huang CX, Yang G, Gao YL, Wu SD, Zhang ZF. Mater Sci Eng A 2008;485:643.
[32] Wang YM, Chen MW, Zhou FH, Ma E. Nature 2002;419:912.
[33] Wang YM, Ma E. Acta Mater 2004;52:1699.
[34] Byun TS, Lee EH, Hunn JD. J Nucl Mater 2003;321:29.
[35] Byun TS. Acta Mater 2003;51:3063.
[36] Meyers MA, Vöhringer OV, Lubarda VA. Acta Mater 2001;49:4025.
[37] Talonen J, Hänninen H. Acta Mater 2007;55:6108.
[38] Kibey S, Liu JB, Johnson DD, Sehitoglu H. Acta Mater 2007;55:6843.
[39] Johnson GR, Cook WH. Eng Fract Mech 1985;21:31.
[40] Venables JA. J Phys Chem Solids 1964;25:693.
[41] Li YS, Zhang Y, Tao NR, Lu K. Acta Mater 2009;57:761.
[42] Chan SY, Yong MP, Yeon SJ, Young KL. Scr Mater 2008;59:71.
[43] Das A, Sivaprasad S, Ghosh M, Chakraborti PC, Tarafder S. Mater Sci Eng A 2008;486:283.
[44] Mirzadeh H, Najafizadeh A. Mater Charact 2008;59:1650.